Nonreciprocal optical links based on time-modulated nanoantenna arrays: Full-duplex communication

Mohammad Mahdi Salary, Samad Jafar-Zanjani, and Hossein Mosallaei*
Metamaterials Lab, Electrical and Computer Engineering Department, Northeastern University, Boston, Massachusetts 02115, USA

(Received 18 May 2018; published 11 January 2019)

Interference of transmitted and received signals hinders the simultaneous functionality of a conventional optical antenna as a transmitter and receiver which is required for full-duplex communication. The full-duplex communication schemes enabled by dense wavelength division multiplexed optical networks require distinct transmitter/receiver components operating at different wavelengths which increase the cost, complexity, and footprint of the physical layer. In this work, we demonstrate that an array of nanoantennas with leaky-wave architecture based on spatiotemporal modulation establishes nonreciprocal optical links which can reject the interference of transmitted and received signals by isolating the frequency of transmission and reception modes. For this purpose, we integrate indium-tin oxide into plasmonic nanodipoles which allows for realization of time-modulated nanoantennas in near-infrared frequency regime through electrical modulation of charge carrier density with radio-frequency signals. The radiation characteristics of individual nanoantennas and modal properties of nanoantenna arrays are rigorously studied through linking of charge transport and electromagnetic models. To this end, we extend the formulation of discrete dipole approximation as the standard modeling tool for electromagnetic scattering from nanoantenna arrays to treat realistic time-modulated structures with drastically different timescales between optical and modulation frequencies. The operation of spatiotemporally modulated array antennas in transmission and reception modes is investigated. Moreover, electrical beam-scanning functionality and dependence of antenna characteristics to modulation parameters and wavelength are demonstrated. It is rigorously established that such array antennas can operate as full transceivers by separating the transmitted and received signals propagating along the same direction through down conversion and up conversion of the frequency. Our results provide a route toward realization of optical antenna systems capable of full-duplex communication and real-time beam scanning which can increase the capacity and decrease the complexity of optical networks.

DOI: 10.1103/PhysRevB.99.045416

Antenna theory is very well established in the radio frequency (RF) and microwave regime [1]. Different design paradigms such as phased array, holographic leaky-wave, and Yagi-Uda antennas have been adopted toward tailoring the radiation pattern, gain, and bandwidth of antennas for many different applications with profound impact on modern information and communication technology. The recent advances in nanofabrication have allowed for downscale of the antenna footprints into nanoscale, enabling high-speed wireless communications in optical frequencies. The new class of plasmonic nanodipoles, consisting of two plasmonic nanoparticles separated by a small gap, has received great attention and the effects of adjusting length, loading, and geometry on tuning the radiation characteristics of nanodipoles have been investigated [2–5]. These nanodipoles can be fed through free-space illumination or optical nanowaveguides and the nanogap region can be used as the transmitting and receiving point of the nanoantenna [6]. Several efforts have been put into translating the well-established concepts of RF antennas into the optical counterparts and different paradigms of reflect-array [7], Yagi-Uda [8], and leaky-wave [9] antennas have been successfully brought into optics by considering an ensemble of plasmonic nanoantennas.

Constrained by the reciprocity, conventional antennas are bound to transmit or receive equally toward or from the same direction at the same frequency. This symmetry between the transmit (Tx) and receive (Rx) modes prohibits functionality of a conventional antenna as a simultaneous transmitter/receiver (transceiver) due to the interference of transmitted and received signals and leads to simplex communication as shown in Fig. 1(a).

However, for most practical applications a full-duplex communication is required to increase the link capacity. In the near-infrared (NIR) regime, dense wavelength division multiplexing (WDM) has allowed for integration of more than 80 channels at several gigahertz intervals from 1530 nm to 1565 nm (C band) via optical splitter/combiners into a single strand multimode optical fiber [10,11]. This approach enables full-duplex communication by dividing the communication channel and using different wavelengths for transmission and reception. However, requirement for distinct receivers and transmitters for each wavelength at each side of the link makes this scheme ineffective in cost and size while adding complexities in implementation of the physical layer [Fig. 1(b)]. In this work, we aim at achieving full-duplex communication in the NIR regime through interference rejection of transmitted and

*hosseinm@ece.neu.edu

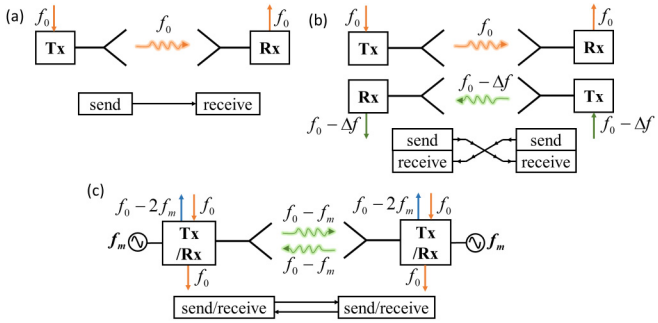

FIG. 1. (a) Simplex communication scheme using an individual antenna at each communication node. (b) Full-duplex communication scheme enabled by wavelength division multiplexing and distinct transmitter/receivers at each communication node. (c) Full-duplex communication by isolating transmission and reception frequencies based on individual antenna with spatiotemporal modulation at each node.

received signals via nonreciprocal optical links in a shared transmission medium as shown in Fig. 1(c) by utilizing an individual leaky-wave antenna consisted of an array of time-modulated nanoantennas.

In order to break the reciprocity, an effective motion is required within the device to enable different behaviors for the waves propagating in forward and backward directions by imparting different momentums to the light. Magneto-optical effects have been traditionally used for this purpose, where a DC magnetic field induces a molecular momentum bias resulting into an asymmetric permittivity tensor [12–15]. This approach requires utilization of bulky and heavy magnets which increases footprint of the device. More recently, exploiting spatiotemporal modulation [16] and material nonlinearities [17,18] have been proposed to realize magnetless nonreciprocal devices with compact footprints suitable for on-chip applications. The linear nonreciprocity based on spatiotemporal modulation is typically stronger than nonlinear reciprocity and enables nonreciprocal response for simultaneous excitations with arbitrary intensities, while nonlinear nonreciprocity requires high intensities and operates for one excitation at a time [19]. This is due to the fact that nonlinear processes and their frequency conversion efficiency are strongly dependent on the intensity of input field. A spatiotemporal modulation of refractive index induces a momentum bias at a macroscopic scale which can be used to mimic the motion of a traveling wave. This approach has been used in waveguide geometries to achieve power isolation [20,21] and to realize nonreciprocal communication with leaky-wave antenna architecture [22–24]. Moreover, space-time gradient metasurfaces have been shown to enable new functionalities and extend the degree of light manipulation beyond the capabilities of static and quasistatic metasurfaces [25–31]. In Refs. [22] and [23], magnetless nonreciprocal leaky-wave antennas in RF have been fabricated by using varactors for applying spatiotemporal modulation. The realization of the concept in the low-THz regime has also been demonstrated using externally biased graphene sheets [24]. Moving beyond THz into infrared and visible frequencies allows for further miniaturization of antenna footprints and enables higher speed in communications due to the higher frequency of carrier waves. However, bringing the concepts from RF into nano-optics requires identification of novel routes to achieve time modulation at optical frequencies as well as modification of analysis and design rules. For this purpose, field-effect modulation in transparent conductive oxides or transition-metal nitrides yields a great promise for realization of time-modulated nanoantennas as it enables electrical modulation of refractive index with several GHz in speed via changes in carrier density and offers a continuous tunability in a relatively wide range with very low power consumption in the steady state [32,33]. Indium-tin oxide (ITO) is one of the most widely used transparent conducting oxides and it has been recently integrated into optical metasurfaces for achieving tunability, switching, and modulation of electromagnetic waves in the NIR regime [33–37]. Despite the real-time tunability offered by these metasurfaces, their operation has remained quasistatic as their variations in time are disregarded.

In this paper, we integrate ITO as an electro-optical load into a plasmonic nanodipole. Radiation characteristics of the nanodipole can be tuned in the NIR regime by applying an external voltage which subsequently changes the carrier concentration and refractive index in the active layer of ITO. Biasing the nanodipole with an RF signal, a time-modulated nanodipole is realized and as a result, the input energy is coupled into higher-order frequency harmonics consisted of the central frequency up- and down-modulated by the modulation frequency. A spatiotemporally modulated leaky-wave antenna is implemented by using an ensemble of time-modulated nanodipoles and applying a progressive phase delay in the temporal modulation of the elements. The operation of antenna in Tx and Rx modes is investigated and it is demonstrated that such an array antenna enables full-duplex communication through a shared transmission medium by isolating transmission/reception frequencies at each port which rejects the interference of transmitted and received signals. In particular, the transmitted and received signals propagating along the same direction can be separated through frequency down-conversion and up-conversion operations. Moreover, the antenna can perform dynamic beam scanning with 180° angle-of-view through electrical tuning of the progressive phase delay in temporal modulation via RF phase shifters. For analyzing the optical response of antenna structures, we extend discrete dipole approximation (DDA) formulation based on a multifrequency approach which allows for efficient and accurate characterization of realistic time-modulated structures with drastically different timescales between optical and modulation frequencies. Moreover, the electro-optical response of nanoantennas is rigorously characterized by linking charge transport and electromagnetic models via carrier-dependent dispersion model. The contributions of our paper are therefore twofold: First, we develop a novel formulation for solving active optical antennas with multiscale spatiotemporal features and second, we implement a spatiotemporally modulated array antenna in the NIR frequency regime capable of performing full-duplex communication by exploiting electro-optical property of ITO. The rest of this paper is organized as follows. In Sec. I, we develop the multifrequency DDA formulation for modeling time-modulated nanoantennas. In Sec. II, we study the radiation characteristics of ITO-loaded

plasmonic nanodipoles. The modal properties of nanoantenna array is discussed in Sec. III and the nonreciprocal behavior of the antenna in Rx and Tx modes is investigated to establish its applicability for full-duplex communication. Moreover, the beam-scanning functionality and dependence of antenna characteristics to modulation parameters and wavelength are presented. Finally, the conclusions are drawn in Sec. IV.

I. FORMULATION

DDA and polarizability theory have been extensively used as the standard modeling tools for analyzing individual nanoantennas as well as nanoantenna arrays and chains of plasmonic particles [9,38–46]. In the level of individual element analysis, DDA is a numerically exact method and equivalent to the method of moments (MoM) solution to the volume integral equation (VIE) formulation of Maxwell's equations [47–51]. In the spirit of volumetric MoM, the volume of the element is discretized into a grid of deeply subwavelength cubical subvolumes each of which is described by a dipolar polarizability. The polarizability of an infinitesimal subvolume is given by the Clausius-Mossotti (CM) expression [52,53]. For a finite cell size, CM polarizability is modified by lattice dispersion relation (LDR) in order to satisfy the optical theorem and increase the accuracy and convergence rate of the results [49,54]. DDA method has been successfully applied to arbitrary-shaped scatterers made of plasmonic [55] and high-index materials [41]. The derivation of DDA equations from VIE formulation of Maxwell's equations is briefly recalled in Sec. 1 of the Supplemental Material [56].

In the level of array analysis, when the dimensions of constituent elements of the array are much smaller than the scattered wavelength, the optical response of each element is dominated by the radiation due to the induced dipolar modes and contribution of higher order multipoles are negligibly small [41,46]. As such, each element can be assigned a polarizability tensor which relates the net induced dipole moment of the element to the local field at its phase center [46,57] and the total scattered field can be subsequently obtained by solving for the induced dipole moments within the framework of DDA. This approach dramatically reduces the number of unknowns to be solved for since the fine meshing of each nanoantenna is replaced by its dipolar polarizability. Such model order reduction, from computational point of view, falls into the category of projection methods in which one seeks for an approximate solution to the full-order problem through projection of integral equations onto a reduced order space. Different projection methods have been used in the framework of MoM such as characteristic basis function method [58], synthetic basis function method [59], and macrobasis function method [60,61]. The accuracy of these methods depends on the proper construction of the projection space which consists of the dipolar polarizability of the elements in the DDA framework. Several techniques have been proposed for polarizability tensor retrieval of subwavelength elements. Among these techniques, the ones based on quasistatic models fail to take into account the energy conservation, radiative damping, and exotic wave phenomena [62–64]. In order to accurately predict the scattering of an element in an array configurations, the dynamic polarizability is required which can be rigorously retrieved via numerical simulations and evaluation of the net induced dipole moment or the scattered field from the element under different incident conditions [46,65]. This approach has been extensively used for homogenization of metamaterials consisting of plasmonic or high-index dielectric and magnetodielectric inclusions with complex geometries [42,46], which yields accurate results in the account of preserved coupling information between the elements while imposing a fraction of computational cost compared to the full-order problem. In particular, DDA framework can be used hierarchically in two different length scales of individual element and array configuration to retrieve the dynamic polarizability of individual nanoantennas [41] and subsequently use the retrieved polarizabilities for solving the scattering from the whole array [44].

Simulation of realistic time-modulated devices in optical frequencies poses a great challenge for conventional time-domain methods such as finite-difference time-domain (FDTD) due to very large difference between timescales of optical and modulation frequencies. The accessible modulation frequencies of electro-optical material are less than 100 GHz which are very small compared to the optical excitation frequencies [20,28]. This requires an enormous number of optical cycles in time-domain simulations to capture the steady-state response, making the computation prohibitive. In the case of nanoantennas with deeply subwavelength features, this becomes even more challenging as the time step in FDTD simulations decreases by decreasing the mesh size. In order to overcome these limitations, multifrequency techniques in frequency domain have been recently proposed [29,31,66] which can capture the stationary-state response of such modulated systems, efficiently and accurately through coupling frequency-domain simulations at different frequency harmonics.

Here, we extend DDA formulation based on a multifrequency approach for treating time-modulated nanoantennas and arrays in the frequency domain. As the starting point, we consider a scatterer discretized into an ensemble of N deeply subwavelength cubical subvolumes whose permittivities are varying in time. When the temporal modulation is sufficiently slow with respect to the oscillations of optical excitation (adiabatic regime), for any given optical frequency, the change in the permittivity of a dispersive material at excited frequency harmonics of different orders is negligible and the main dispersion effects arise from the optical excitation. In such a case, the stationary-state scattering response in the frequency domain can be obtained by solving for a nondispersive time-varying material at each optical frequency. The validity of this assumption is guaranteed in the real-case scenarios at the optical frequency regime where modulation frequency is a very small fraction of excitation frequency. The time-dependent CM polarizability tensor of the nth cell at the optical frequency of ω_0 can be obtained as [52]:

$$\underset{d_n\to 0}{\bar{\bar{\mathfrak{a}}}_n(t)} = \bar{\bar{I}}\mathfrak{a}_n^{\mathrm{CM}}(t) = \bar{\bar{I}}d_n^3\frac{3}{4\pi}\frac{\epsilon_n(t)-1}{\epsilon_n(t)+2}, \tag{1}$$

where d_n and ϵ_n are the dimension and time-dependent permittivity at optical frequency of ω_0 corresponding to the nth dipolar cell, respectively, and $\bar{\bar{I}}$ is the identity dyadic. The

CM polarizability is subsequently modified by higher-order correction terms through LDR in order to satisfy the optical theorem and improve the accuracy and convergence for a finite cell size [49]:

$$\begin{aligned}\bar{\bar{\mathfrak{a}}}_n(t) = \bar{\bar{I}}\mathfrak{a}_n^{\mathrm{CM}}(t)\big[1 - \big(\mathfrak{a}_n^{\mathrm{CM}}(t)/d_n^3\big) \\ \times \big[\big(b_1^{\mathrm{LDR}} + b_2^{\mathrm{LDR}}\epsilon_n(t) + b_3^{\mathrm{LDR}}\epsilon_n(t)S\big)(k_0 d)^2 \\ + (2/3)i(k_0 d)^3\big]\big]^{-1},\end{aligned} \tag{2}$$

where $b_1^{\mathrm{LDR}} \approx 1.8915$, $b_2^{\mathrm{LDR}} \approx -0.1648$ and $b_3^{\mathrm{LDR}} \approx 1.77$ are LDR constants, k_0 is the free-space wave number, and $S = \sum_{\mu=1}^{3}(\hat{a}_\mu \hat{e}_\mu)^2$ with $\hat{a}$ and $\hat{e}$ being the unit vectors denoting direction of propagation and polarization of the incident field ($\vec{E}_{\mathrm{inc}}$), respectively. When the elements are varying in time with a periodic modulation having a modulation frequency of ω_m, the time-dependent polarizability is also periodic and can be expanded in the form of a Fourier series as:

$$\bar{\bar{\mathfrak{a}}}_n(t) = \sum_l \bar{\bar{\alpha}}_n^l(\omega_0)e^{il\omega_m t}, \tag{3}$$

and the Fourier transform takes the following form:

$$\bar{\bar{\alpha}}_n(\omega) = \sum_l \bar{\bar{\alpha}}_n^l(\omega_0)\delta(\omega - l\omega_m). \tag{4}$$

Disregarding the dispersion effects arising from adiabatically generated frequency harmonics, the temporal evolution of the dipole moment corresponding to the nth cell [$\vec{\mathfrak{P}}_n(t)$] can be expressed as:

$$\vec{\mathfrak{P}}_n(t) = \bar{\bar{\mathfrak{a}}}_n(t)\vec{\mathfrak{E}}(\vec{r}_n, t), \tag{5}$$

where $\vec{\mathfrak{E}}(\vec{r}_n, t)$ is the time-dependent external electric field at the phase center of the nth dipole denoted by the coordinate vector of $\vec{r}_n$.

The dipolar equation can be taken into angular frequency domain by taking the Fourier transform of both sides as:

$$\begin{aligned}\vec{p}_n(\omega) &= \bar{\bar{\alpha}}_n(\omega) * \vec{E}(\vec{r}_n, \omega) \\ &= \int \bar{\bar{\alpha}}_n(\omega - \omega')\vec{E}_n(\vec{r}_n, \omega')d\omega',\end{aligned} \tag{6}$$

where * denotes convolution. This equation implies that an input frequency of ω_0 will excite dipole moments corresponding to a spectrum of output frequencies. Substituting Eq. (4) into (6) while choosing $\omega = \omega_q = \omega_0 + q\omega_m$ and $\omega' = \omega_p = \omega_0 + p\omega_m$ with $q, p = \cdots, -1, 0, +1, \cdots$, we will arrive at the following coupled multifrequency equations, relating the induced dipole moments of output spectrum to the local field of input spectrum at the nth lattice point:

$$\{\vec{p}_n(\omega_q)\} = \{\bar{\bar{\alpha}}_n^{q-p}(\omega_0)\}\{\vec{E}(\vec{r}_n, \omega_p)\}, \tag{7}$$

in which the local field can be expressed as the sum of incident field and the sum of scattered fields from all other dipoles as:

$$\vec{E}(\vec{r}_n, \omega_p) = \vec{E}_{\mathrm{inc}}(\vec{r}_n, \omega_p) + \sum_{\substack{m=1 \\ m\neq n}}^{N} \bar{\bar{G}}(\vec{r}_{nm}, \omega_p)\vec{p}_m(\omega_p), \tag{8}$$

where $\vec{r}_{nm} = \vec{r}_n - \vec{r}_m$ and $\bar{\bar{G}}(\vec{r}_{nm}, \omega_p)$ is the free-space dyadic Green's function, giving the free-space electric field at $\vec{r}_n$ due to radiation from an infinitesimal dipole at $\vec{r}_m$ with a frequency of ω_p:

$$\bar{\bar{G}}(\vec{r}_{nm}, \omega_p) = \big(k_p^2\bar{\bar{I}} + \nabla\nabla\big)\frac{\exp(ik_p|\vec{r}_{nm}|)}{|\vec{r}_{nm}|}, \tag{9}$$

where $k_p = \omega_p/c$. Writing the coupled equations (7) and (8) for all dipoles ($n = 1, \cdots, N$), we will obtain a linear system of equations in the following form:

$$\overline{p} = \bar{\bar{T}}\,\overline{E}_i, \tag{10}$$

whose solution gives the induced dipole moments of each cell corresponding to different frequency harmonics. In the above equation, $\overline{p} = [\overline{p}_1, \overline{p}_2, \cdots, \overline{p}_N]^T$ with:

$$\overline{p}_n = [\cdots, \vec{p}_n(\omega_{-1}), \vec{p}_n(\omega_0), \vec{p}_n(\omega_{+1}), \cdots]^T, \tag{11}$$

and $\overline{E}_i = [\overline{E}_{i,1}, \overline{E}_{i,2}, \cdots, \overline{E}_{i,N}]^T$ with:

$$\overline{E}_{i,n} = [\cdots, \vec{E}_{\mathrm{inc}}(\vec{r}_n, \omega_{-1}), \vec{E}_{\mathrm{inc}}(\vec{r}_n, \omega_0), \vec{E}_{\mathrm{inc}}(\vec{r}_n, \omega_{+1}), \cdots]^T, \tag{12}$$

and

$$\bar{\bar{T}} = \begin{bmatrix} \bar{\bar{T}}_{1,1} & \bar{\bar{T}}_{1,2} & \cdots & \bar{\bar{T}}_{1,N} \\ \bar{\bar{T}}_{2,1} & \bar{\bar{T}}_{2,2} & \cdots & \bar{\bar{T}}_{2,N} \\ \vdots & \vdots & \ddots & \vdots \\ \bar{\bar{T}}_{N,1} & \bar{\bar{T}}_{N,2} & \cdots & \bar{\bar{T}}_{N,N} \end{bmatrix}$$

with:

$$\bar{\bar{T}}_{\substack{n,m \\ n=m}} = \begin{bmatrix} \ddots & \vdots & & \iddots \\ & \bar{\bar{\alpha}}_n^0 & \bar{\bar{\alpha}}_n^{-1} & \bar{\bar{\alpha}}_n^{-2} & \\ \cdots & \bar{\bar{\alpha}}_n^{+1} & \bar{\bar{\alpha}}_n^0 & \bar{\bar{\alpha}}_n^{-1} & \cdots \\ & \bar{\bar{\alpha}}_n^{+2} & \bar{\bar{\alpha}}_n^{+1} & \bar{\bar{\alpha}}_n^0 & \\ \iddots & \vdots & & \ddots \end{bmatrix}^{-1}, \tag{13}$$

$$\bar{\bar{T}}_{\substack{n,m \\ n\neq m}} = -\begin{bmatrix} \ddots & & & & \\ & \bar{\bar{G}}(\vec{r}_{nm}, \omega_{-1}) & & & \\ & & \bar{\bar{G}}(\vec{r}_{nm}, \omega_0) & & \\ & & & \bar{\bar{G}}(\vec{r}_{nm}, \omega_{+1}) & \\ & & & & \ddots \end{bmatrix} \tag{14}$$

The structure of self-interaction blocks in the interaction matrix implies that introducing a periodic time modulation with a modulation frequency of ω_m leads to generation of all frequency harmonics $\omega_0 \pm q\omega_m$ due to self-coupling effects. For a time-invariant subvolume, $\bar{\bar{\alpha}}_n^{q-p} = \bar{\bar{\alpha}}_n(\omega_p)\delta_{qp}$ in which δ_{qp} is the Kronecker delta that decouples the frequency harmonics. Truncating the number of frequency harmonics at $\pm M_f$, the size of matrix equation (10) will be $3N(2M_f + 1)$. Compared to the conventional DDA method, multifrequency DDA leads to generation of larger interaction matrices [$\times(2M_f + 1)$], however, it should be noted that the generated matrices are sparse unlike the dense matrices of conventional DDA. This is due to the decoupled interaction of frequency harmonics via Green's functions. According to the block structures in equations (13) and (14), it can be

easily concluded that the density of interaction matrix in multifrequency DDA is less than $\frac{N+2M_f}{N(2M_f+1)}$. The sparsity of the interaction matrix in multifrequency DDA can be exploited to decrease the storage requirements and accelerate the matrix-vector multiplications in iterative solvers via sparse operations. For further reduction of the computational complexity and memory consumption, fast Fourier transform (FFT) [67] and Hierarchical matrix ($\mathbb{H}$-matrix) construction [68] can be adopted similar to the conventional DDA formulation.

Once the dipole moments of the subvolumes in an individual scatterer are obtained at different frequency harmonics, the contributions of multipole modes to the scattering at all frequency harmonics can be extracted through Taylor expansion of the fields around the phase center of the scatterer [41]. In particular, the scattering response of a deeply subwavelength nanoantenna is dominated by the contribution of dipolar modes whose net dipole moments at different frequency harmonics can be obtained as $\vec{P}(\omega_q) = \sum_{i=1}^{N} \vec{p}_i(\omega_q)$. By extracting the net dipole moments of a nanoantenna under three independent incident conditions (e.g., plane wave excitations along three principal axes), each block of the corresponding multifrequency dynamic polarizability tensor can be rigorously retrieved, as:

$$\left\{\overline{\overline{\alpha}}^{q-p}(\omega_0)\right\} = \{\vec{P}_1(\omega_q) \quad \vec{P}_2(\omega_q) \quad \vec{P}_3(\omega_q)\} \times \{\vec{E}_1(\omega_p) \quad \vec{E}_2(\omega_p) \quad \vec{E}_3(\omega_p)\}^{-1}, \qquad (15)$$

This polarizability relates the net induced dipole moments of the nanoantenna at the output spectrum to the local field of input frequency spectrum at the phase center of nanoantenna. Subsequently, an array of subwavelength time-modulated nanoantennas can be solved within the same framework of multifrequency DDA by replacing the fine meshing of each nanoantenna by its retrieved polarizability. This approach relaxes the computational requirements for solving large-scale array problems which are intractable by adopting conventional computational techniques, while yielding accurate results for the scattered fields as the coupling information between the elements are preserved. Solving the matrix equation (10) for an array of subwavelength time-modulated nanoantennas described by their position and multifrequency dynamic polarizabilities, the net dipole moments of each nanoantenna at different frequency harmonics will be obtained which allows for straightforward calculation of the scattered fields of different frequency harmonics via dyadic Green's functions.

It should be mentioned that the periodicity can be simply considered in the developed formulation by using the periodic dyadic Green's functions evaluated by Ewald's method [69]. The substrate contribution can also be taken into account by incorporating the dyadic Green's functions of layered media to via discrete complex image method (DCIM) to avoid meshing of the substrate volume [70]. The formulation can also be readily extended for treatment of magnetic dipoles in high-index dielectric nanoantennas and the magneto-electric cross coupling in chiral geometries [44,69].

The validity and accuracy of the developed formulation is rigorously verified in Sec. 2 of the Supplemental Material [56] by comparing the near-field and far-field results of generated frequency harmonics by a time-modulated nanodipole obtained with multifrequency DDA and full-wave simulation results of FDTD. Moreover, the superior computational performance of the method in characterization of the steady-state response of time-modulated structures with multiscale temporal and spatial features is established.

II. ITO-LOADED PLASMONIC NANODIPOLE

Recently, several different approaches have been proposed to change the refractive index of materials by using external stimuli which enable dynamic functionality and real-time tunability of the optical response. In the NIR regime, mechanical reconfiguration [71], phase transitions [72], and carrier accumulation/depletion [33] have been utilized for this purpose. Among all these mechanisms, field effect modulation is the most promising approach for realization of time-modulated nanoantennas as it allows for continuous tunability of refractive index over a relatively wide range with modulation speeds up to several GHz while possessing very low power consumption. It has been recently used in transparent conducting oxides [33] and transition metal nitrides [73] to achieve tunability in NIR and visible frequencies by integration of these materials into resonant geometries. When such electro-optical materials are biased in a parallel capacitor configuration, a driving static electric field forms an ultrathin charge accumulation or depletion layer at the interface of material with the insulator depending on the sign of applied voltage [74]. The changes in carrier concentration within the accumulation/depletion layer can be subsequently translated to the changes in complex dielectric function using carrier-dependent dispersion models. By applying an RF biasing signal, the carrier concentration and thus the dielectric function can be modulated in time with speeds up to several GHz [20,32,33]. The maximum speed of modulation is limited by the signal delay resulting from RF probe connections, with current speed values up to $\approx$100 GHz [75].

Here, we consider a plasmonic nanodipole as the basic radiating element. The geometry of nanoantenna is depicted in Fig. 2(a), which consists of rectangular arms made of silver with a length of L, width of w, and height of h. The nanodipole is loaded with an ITO layer and a silica insulating layer at its gap with thicknesses of g_{ITO} and $g_{\mathrm{SiO_2}}$, respectively, in accordance with biasing requirements. Large enhancement of electric field at the gap of nanoantenna when it is operating at the resonant wavelength, enhances light-matter interactions at nanoscale and provides a route to achieve a large tunability by the slightest changes in the refractive index of the nanoload [3,5]. As such, integration of ITO into the nanogap enables real-time tuning of nanoantenna radiation characteristics in the NIR regime through applying a DC bias via its electro-optical property. Moreover, it allows for realization of time-modulated nanoantennas by applying an RF biasing signal. The electro-optical response of nanoantenna is characterized through linking of charge transport and electromagnetic models. The charge transport is modeled using Lumerical Device simulator, which solves drift-diffusion and Poisson equations self-consistently based on a finite-element method, while the electromagnetic modeling is carried out based on the multifrequency DDA method by discretizing the volume of

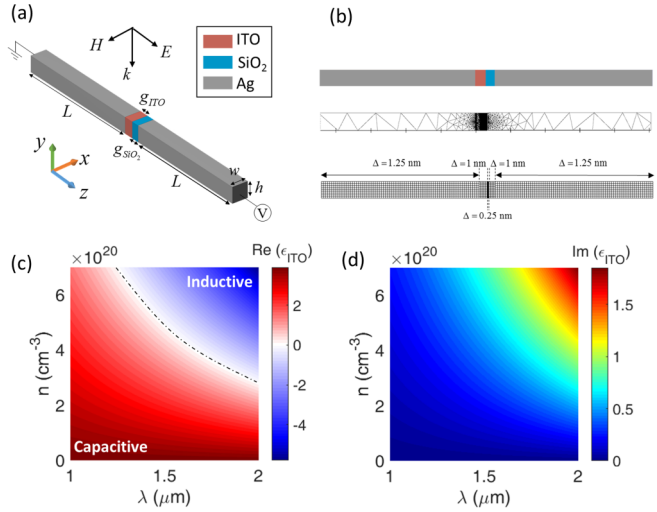

FIG. 2. (a) The schematic of an ITO-loaded plasmonic nanodipole. (b) Typical multiscale meshes used for FEM device (triangular mesh) and DDA electromagnetic (cubic mesh) simulations. (c) and (d) demonstrate real and imaginary parts of ITO permittivity as functions of wavelength and carrier concentration, respectively.

nanoantenna into cubic dipolar cells in the spirit of VIE methods. In both device and electromagnetic simulations, a multiscale meshing is adopted with refined mesh at the interface of ITO and insulator to capture the decay length of charge accumulation/depletion layer as well as the large field confinement at the nanogap, accurately and efficiently. It has been shown previously that a nonuniform mesh improves the convergence of the DDA method for solving structures with nanogaps and deeply subwavelength features [76,77]. Moreover, the convergence of the DDA is much faster for cubically-shaped objects due to the absence of shape reconstruction errors with cubical subvolumes. Figure 2(b) depicts the typical multiscale meshes used for device and electromagnetic simulations.

The complex-valued permittivity of silver is taken from experimentally obtained results [78] and the dielectric function of ITO is described by a Drude model as [33]:

$$\epsilon_{\mathrm{ITO}}(\omega, n) = \epsilon_{\mathrm{inf}} - \frac{ne^2}{\epsilon_0 m^* m_0} \frac{1}{\omega^2 + i\omega\Gamma}, \qquad (16)$$

where $\epsilon_{\mathrm{inf}} = 3.9$ is the high-frequency dielectric constant, n is the carrier concentration, e is electron charge, ϵ_0 is the vacuum permittivity, $m^* = 0.35$ is the effective mass of charge carrier, m_0 is the electron mass, ω is the angular frequency, and $\Gamma = 1.8 \times 10^{14}$ rad/s is the damping constant [33,79]. Figures 2(c) and 2(d) demonstrate the real and imaginary parts of ITO permittivity as functions of wavelength and carrier concentration. As can be seen, increasing the carrier concentration leads to decrement of the real part of permittivity. In particular, the permittivity crosses zero in the NIR regime by increasing the carrier concentration such that the optical behavior of nanoload is changed from capacitive (dielectric) to inductive (plasmonic).

In the device simulations, ITO is modeled as a semiconductor with the DC permittivity of $\epsilon_{\mathrm{DC}} = 9.3$ [80], band gap of $E_{\mathrm{bg}} = 2.8$ eV [81], and electron affinity of $\chi = 5$ eV [33].

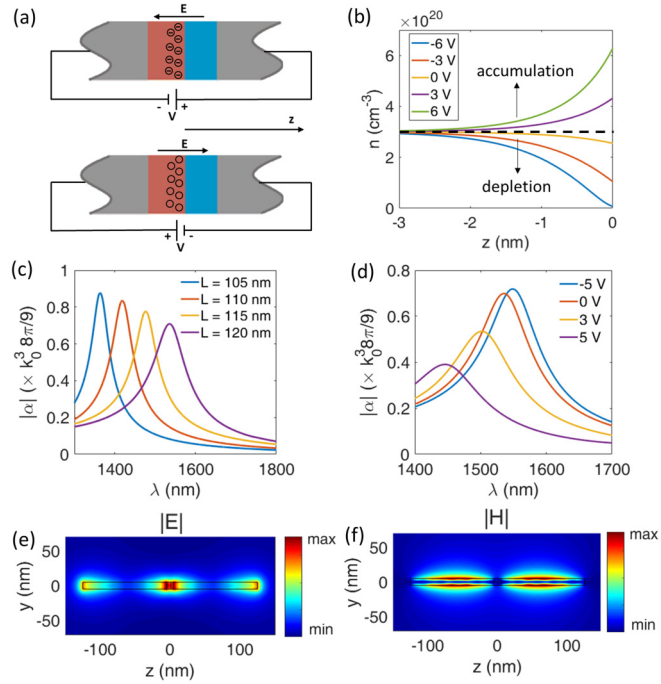

FIG. 3. (a) Schematic representation of charge accumulation and depletion at the ITO-SiO_2 interface upon applying bias voltages with different signs. (b) The spatial distribution of carrier concentration as a function of position with respect to the ITO-SiO_2 interface for different applied bias voltages. (c) The normalized polarizability of unbiased ITO-loaded nanodipole as a function of wavelength for different arms lengths. (d) The normalized polarizability of ITO-loaded nanodipole with arm length of $L = 120$ nm as a function of wavelength for different applied bias voltages. (e) and (f) demonstrate distribution of electric and magnetic fields at the resonant wavelength of unbiased ITO-loaded nanodipole with $L = 120$ nm.

In the following, we study the radiation characteristics of quasistatic and time-modulated ITO-loaded plasmonic nanodipoles.

A. Quasistatic Nanoantenna

We consider a nanodipole with $w = h = 10$ nm, $g_{\mathrm{ITO}} = 6$ nm, and $g_{\mathrm{SiO_2}} = 4$ nm. Figure 3(a) schematically depicts the field-effect induced charge accumulation and depletion mechanism under applied external biases of different signs. The sign of applied voltage determines the direction of static electric field and the electron charge carriers will be driven opposite to that direction which results into accumulation/depletion. A background carrier concentration of $n_{\mathrm{bg}} = 3 \times 10^{20}$ cm^{-3} is considered for the n-doped ITO layer [33]. The carrier concentration within the ITO layer as a function of position with respect to ITO/SiO_2 interface is obtained using Lumerical solver and is plotted in Fig. 3(b) for different DC applied bias voltages. As can be observed, a negative bias voltage results in depletion of charges at the interface while a positive bias voltage leads to formation of an accumulation layer. The slight depletion of charges occurred at 0 V bias is due to the lower work function of degenerately doped ITO compared to that of silver [33]. The spatial charge distribution in depletion/accumulation layer exhibits an exponential decay

profile with a decay length of ≈2.5 nm. This distribution can be translated into an inhomogeneous permittivity profile using the Drude model in equation (16). To bring out the essential physics effectively and relax the mesh refinement required for convergence of computational results, the carrier concentration is taken to change homogeneously in an effective active region with a thickness of 1 nm which is shown to provide fairly accurate results consistent with the inhomogeneous distribution [37].

The nanodipole is illuminated by a normally incident plane wave with polarization along the arms, as shown in Fig. 2(a). The scattering from nanoantenna is analyzed using DDA and the polarizability tensor of nanoantenna is retrieved as outlined in Sec. I. The dominant component in the polarizability tensor of the nanoantenna is α_{zz} and other components are small due to the absence of polarization cross coupling and the ultrathin dimensions of nanodipole along the x and y directions. As such, in the rest of this paper, polarizability of nanoantenna refers to α_{zz} component. Figure 3(c) shows the normalized polarizability of nanoantenna as a function of wavelength for different arm lengths. According to the Mie scattering theory, the maximum value that the polarizability of a resonant dipolar particle can yield is $k_0^3 8\pi/9$ with the notation used in this paper [39]. As such, all the polarizabilities are normalized with a factor of $k_0^3 8\pi/9$ consistent with the approach used in Refs. [2–5]. A resonant peak is observed in the polarizability spectra corresponding to the open-circuit resonance of the nanoantenna [3,5] which is shifted toward longer wavelengths by increasing the arm length. The resonant wavelength is located where the length of nanoantenna is equal to λ_{eff} with λ_{eff} being the effective wavelength of guided light along the nanoantenna. It should be noted that due to the plasmonic features of silver and high confinement of electric field at the nanogap, the effective guided wavelength is significantly smaller compared to the free-space wavelength which results in drastic miniaturization of optical nanoantennas [3]. The radiation efficiency of nanoantenna is enhanced at the resonant wavelength and retains a reasonably high value over a relatively wide spectral range around the resonance. In the rest of our analysis, we choose the arm length as $L = 120$ nm which exhibits the resonance close to the free-space wavelength of $\lambda = 1.55$ μm corresponding to the telecommunication wavelength at the C band. Figure 3(d) demonstrates the polarizability of this nanoantenna as a function of wavelength for different applied bias voltages. As expected, by increasing the voltage, resonance is shifted into shorter wavelengths due to decrement of the permittivity in the active region of ITO layer which decreases the capacitance of nanoload. At the same time, the resonance becomes broader and weaker in the account of increment in the carrier-induced optical loss in the active region of ITO. An opposite trend is observed for negative voltages, where depletion of charges leads to increment of the nanoload capacitance and decrement of carrier-induced optical loss. It can be noted that the resonance experiences smaller spectral shift for negative applied bias voltages due to less significant change in the permittivity of active region of nanoload through depletion of charges. According to Fig. 2(c), depletion of charge carriers will lead to unity-order increment in the real part of permittivity, whereas by increasing the carrier concentration, the real part of permittivity decreases more significantly and crosses zero leading to a substantial change in the light-matter interaction. The wide spectral tunability in the resonant wavelength of the nanodipole is afforded in the account of high field confinement at the nanogap which leads to significant enhancement of light-matter interactions with the active region at nanoscale. The distributions of scattered electric and magnetic fields corresponding to the nanodipole antenna with $L = 120$ nm at the resonant wavelength are plotted in Figs. 4(e) and 4(f), respectively. The field patterns closely resemble that of a radiating current dipole. The electric field is strong at the edges while the highest confinement occurs at the nanogap.

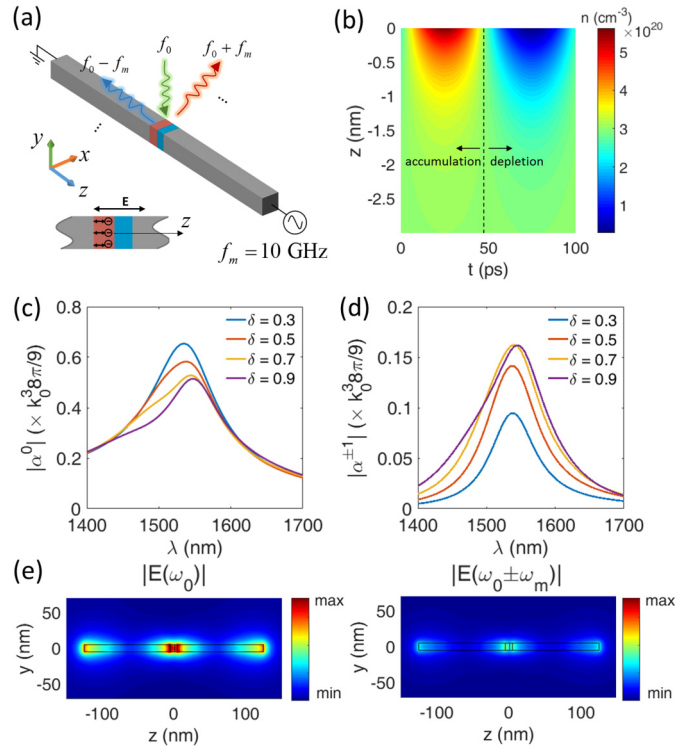

FIG. 4. (a) The schematic of a time-modulated plasmonic nanodipole implemented by carrier modulation of ITO nanoload with an RF signal. (b) The distribution of carrier concentration as a function of position with respect to the ITO-SiO_2 interface and time within one cycle of temporal modulation with a frequency of $f_m = 10$ GHz. (c) and (d) demonstrate normalized polarizability components of time-modulated plasmonic nanodipole as functions of wavelength for different modulation depths, corresponding to the fundamental and first-order frequency harmonics, respectively. (e) depicts distributions of electric field at the resonant wavelength of time-modulated nanodipole corresponding to fundamental and first order frequency harmonics.

B. Time-modulated nanoantenna

Next, we consider the plasmonic nanoantenna biased with a sinusoidal RF signal $v(t) = v_0 \sin \omega_m t$ with modulation frequency of $f_m = 10$ GHz and amplitude of $v_0 = 5$ V as shown schematically in Fig. 4(a). The spatiotemporal distribution of carrier concentration within the ITO layer corresponding to one cycle of temporal modulation is obtained using transient

mode of Lumerical solver and is depicted in Fig. 4(b). As can be seen, the charge distribution has an exponential decay profile in space while it is varying almost sinusoidally in time through consecutive accumulation and depletion. In this case, the carrier concentration in the effective accumulation/depletion layer is taken to vary as $n(t) = n_{\rm bg}(1 + \delta \sin(\omega_m t))$. It should be noted that while carrier concentration and accordingly permittivity have sinusoidal profiles in time, the temporal profile of polarizability corresponding to the subvolumes in the active region of ITO (given by LDR) is nonsinusoidal but is still periodic with the modulation frequency of f_m.

As a result of time modulation and as implied by equations in the formulation section, the input energy to the nanoantenna is coupled to higher-order frequency harmonics ($f_0 \pm nf_m$), where the degree of coupling is determined by the temporal variations in scattering. The polarizability of nanoantenna corresponding to different frequency harmonics is retrieved using multifrequency DDA, as outlined in Sec. I by considering $M_f = \pm 3$ for the maximum number of harmonics which is found to be sufficient for convergence of the results (the amplitudes of higher-order frequency harmonics decay rapidly by increasing the harmonic index such that all other higher-order frequency harmonics are negligibly small). In the account of small modulation frequency compared to the excitation frequency, the up- and down-modulated frequency harmonics are excited with almost equal efficiencies [29]. The nanoantenna polarizability components corresponding to the fundamental and first-order frequency harmonics are plotted in Figs. 4(c) and 4(d) for different modulation depths (δ) of carrier concentration in the active region of ITO layer, respectively. It can be noted that the frequency conversion efficiency to higher order harmonics is proportional to the modulation depth and is maximum in the vicinity of resonant wavelength. This can be understood from the fact that the temporal change in the scattering response of the nanoantenna is maximal around the resonance due to enhanced light-matter interactions and sensitivity via large confinement of the electric field in the active region of nanogap. Furthermore, because of coupling to higher order frequency harmonics, the quality factor corresponding to the fundamental frequency harmonic resonance decreases and the resonant peak becomes broader by increasing the modulation depth.

The electric field patterns corresponding to the fundamental and first-order harmonics are plotted in Fig. 4(e) at the resonant wavelength for the modulation depth of $\delta = 0.9$ which exhibit similar dipolar distribution with the highest field confinement in the nanogap associated with the resonance.

III. NONRECIPROCAL LEAKY-WAVE ANTENNAS

In this section, we study the modal properties of an array of nanoantennas and establish nonreciprocal optical links in the NIR regime using a two-port spatiotemporally-modulated array antenna with leaky-wave architecture in which the radiation is achieved through space-time transition of a guided mode into a leaky-wave mode, while the nonreciprocity of the optical links isolates the frequency of transmission and reception modes of the antenna. This approach allows for full-duplex communication at the NIR regime with a single array antenna in the account of rejection of interference between transmitted and received signals at each port. The major portion of the optical link between the communication nodes consists of the wireless broadcasting link, i.e., the free space between two antenna systems.

The simulation of nanoantenna arrays has been carried out in the framework of multifrequency DDA by retrieving multifrequency dynamic polarizability of individual nanoantennas and replacing the fine meshing of nanoantennas with their dynamic polarizabilities to solve for the induced dipole moments at different frequency harmonics. This reduced order model enables us to bring out the essential physics by neglecting the contribution of higher-order multipoles and yields a good approximation to the full-order model which is demonstrated and discussed in Sec. 3 of the Supplemental Material [56]. In particular, both dipolar and full-order models predict the excitation of guided mode along the array with the same effective wavelength verifying that the excitation of guided modes in such a plasmonic nanoantenna array is indeed a result of collective excitation of dipolar modes in the adjacent elements [38,39,46,82]. It can be concluded that retaining the dipolar couplings is sufficient for an accurate description of the scattering from a chain of transversely polarized plasmonic particles, even for narrow spacings. In the case of transverse polarization, the variation in the scattering response of the elements is very minor by changing the interparticle distance and it is dominated by the dipolar resonance near the wavelength corresponding to the resonance of isolated particles [83–86].

A. Modal properties of nanoantenna array

The modal properties of nanoparticle chains and arrays of nanodipoles have been comprehensively studied [38,39,87]. It has been shown that such arrays may support guided and leaky modes, with longitudinal and transverse polarizations in which the dipole moments of constituent elements are along and perpendicular to the array axis, respectively. These modes are characterized by the complex-valued spatial frequencies along the array direction $k = \beta + i\alpha$. Defining the free-space wave number as $k_0 = \frac{2\pi}{\lambda}$, the modes with $|\beta| < k_0$ are leaky modes which are loosely confined to the array and will radiate into free space, while the modes with $|\beta| > k_0$ are guided modes which propagate along the array with no radiation to free space. Here, we consider an array of unbiased ITO-loaded nanodipoles as shown in Fig. 5(a) which is transversely polarized ($p \perp x$). It has been shown that an array of transversely polarized dipoles supports a backward guided mode ($|\beta_x| > k_0$) [39]. Unlike longitudinal mode (for which $p \parallel x$), the dispersion of transverse backward mode yields $\frac{d\omega}{d\beta_x} < 0$ for $\beta_x > 0$, which is a result of group and phase velocities of guided light being antiparallel. This mode is supported for a range of spacing between nanoantennas smaller than a threshold value. The narrower spacing allowed for transversely polarized nanoantennas, yields higher modal confinement compared to the longitudinally polarized counterparts. Moreover, as the spacing between the nanoantennas decreases, the sensitivity of the mode with respect to ohmic losses decreases and the bandwidth increases [39]. This means that denser arrays are expected to have a better guidance of

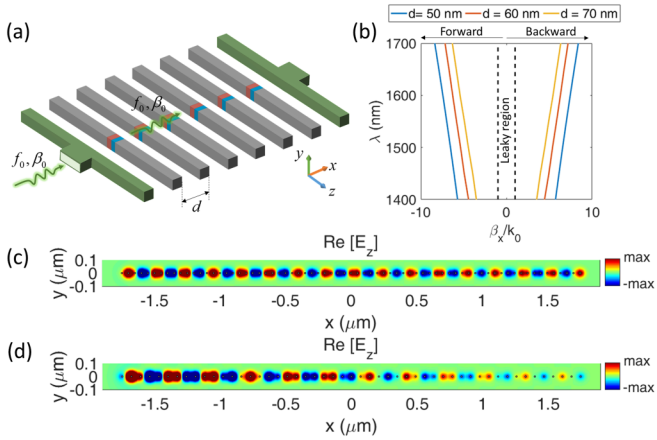

FIG. 5. (a) An array of ITO-loaded plasmonic nanodipoles with a separation distance of d excited by an injected guided mode. (b) The dispersion diagram of supported backward guided modes in an array of unbiased ITO-loaded plasmonic nanodipoles for different nanoantenna spacing. (c) and (d) demonstrate the field distributions of transverse electric field along an array of nanodipoles at the wavelength of $\lambda_0 = 1.55\ \mu$m for different nanoantenna spacings of $d = 50$ nm and $d = 70$ nm, respectively.

energy. The dispersion diagram of the nanoantenna array is obtained using the approach developed in Ref. [39] and the results are plotted in Fig. 5(b) for different spacing between nanoantennas. The dashed lines in Fig. 5(b) denote light lines ($|\beta_x| = k_0$) and the region between them is the leaky (fast-wave) region and the region outside is the guided region. In the account of backwardness of the guided mode, the positive spatial frequencies β_x correspond to the modes with negative group velocity propagating in the $-x$ direction (backward propagation) and the negative spatial frequencies β_x indicate positive group velocity and propagation in the $+x$ direction (forward propagation). As can be observed, by decreasing the spacing between nanoantennas the ratio of $|\beta_x/k_0|$ corresponding to the transverse guided mode supported by the array increases, indicating a higher modal confinement. The near-field distributions of the transverse electric field (E_z) corresponding to the guided modes in an array of nanoantennas with a total length $3.5\ \mu$m and spacings of 50 nm and 70 nm are demonstrated in Figs. 5(c) and 5(d), respectively, in the x-y plane cutting through the center of nanoantennas for the excitation wavelength of $\lambda_0 = 1.55\ \mu$m (since the dipolar approach is only applicable for calculation of scattered fields outside of the elements, the internal fields are excluded in the figures). The results clearly show the better guidance of the denser array as expected. In order to achieve minimal absorption and maximum bandwidth for the guided mode, we choose the spacing between nanoantennas as $d = 50$ nm in the following.

B. Operation modes of spatiotemporally-modulated leaky-wave antenna

Next, we consider the nanoantenna array in which the elements are biased separately with a progressive phase delay in order to realize a spatiotemporal modulation in the carrier concentration of ITO nanoloads such that $n(x,t) = n_{bg}(1 + \delta\cos(\omega_m t - \beta_m x))$. Such modulation mimics a traveling wave along the array whose phase velocity $v_m = \frac{\omega_m}{\beta_m}$ and direction controls the space-time modal transitions via momentum exchange with light. Since the spatial modulation is a phase term for temporal modulation, it can be implemented by using RF phase shifters in the biasing network as shown in Fig. 6(a) to apply temporal modulation with a progressive phase delay of $\beta_m x$. In order to model the spatiotemporally modulated array, we have retrieved the multifrequency dynamic polarizability tensor of the nanoantenna for temporal modulations with different phase delays. The retrieved spectra of polarizability components corresponding to different orders of frequency harmonics are brought in Sec. 4 of the Supplemental Material [56]. The results indicate that applying a phase delay of $\beta_m x$ to the temporal modulation of nanoantenna leads to $\overline{\overline{\alpha}}^p$ experiencing a phase shift of $p\beta_m x$ while maintaining a constant amplitude. This can also be concluded from multifrequency DDA equations in which a shift in the time-domain polarizabilities is mapped to a phase shift in their Fourier coefficients in the frequency domain (see Sec. 4 of the Supplemental Material [56] for derivation).

It is well established that a spatial modulation allows coupling of guided modes into radiative leaky modes through spatial diffraction [88,89]. In such a case, the dispersion diagram consists of an infinite set of branches, where nth branches are shifted horizontally by $n\beta_m$ with respect to the branches of an unmodulated system and the spatial diffraction orders are defined by temporal and spatial frequencies of $(f, \beta_x) = (f_0, \beta_0 + n\beta_m)$ with (f_0, β_0) denoting frequencies of the input mode. This leads to reciprocity between transmission and reception modes as the coupling of $(f_0, \beta_0) \rightarrow (f_0, \beta_0 - \beta_m)$ dictates the coupling of $(f_0, -\beta_0 + \beta_m) \rightarrow (f_0, -\beta_0)$. The reciprocity constraint is lifted by space-time modal transitions upon introducing a temporal modulation. In this scenario, nth branches of dispersion diagram are shifted horizontally by $n\beta_m$ and vertically by $n\omega_m$ with respect to the branches of unmodulated structure [90]. According to the Floquet theorem for spatiotempotally periodic media [91], the allowed diffraction orders for the system are defined by temporal and spatial frequencies of $(f, \beta_x) = (f_0 + nf_m, \beta_0 + n\beta_m)$. This implies that spatial diffraction to higher-order spatial frequency harmonics is accompanied by a frequency conversion to higher-order temporal frequency harmonics which can isolate the temporal frequency of transmitted and received waves and also break the spatial symmetry between transmission and reception patterns. In the following, we examine the operation of the spatiotemporally modulated array antenna in Tx and Rx modes.

The array is considered to have a total aperture length of $11\ \mu$m consisted of 220 nanoantennas with a separation distance of $d = 50$ nm. The modulation parameters are chosen as $f_m = 10$ GHz, $\beta_m d = -1.55$, and $\delta = 0.9$. The dispersion diagram of this spatiotemporally modulated array antenna is plotted in Fig. 6(b). We study the radiation characteristics of the antenna by feeding the antenna from port 1 (forward propagation) and port 2 (backward propagation). The temporal and spatial frequencies of the input backward guided mode into port 1 are defined by $(f, \beta_x) = (f_0, \beta_0)$ where f_0 is the frequency corresponding to the wavelength of $\lambda_0 = 1.55\ \mu$m and $\beta_0 \approx -7.18k_0$. This point is located on the left-hand side

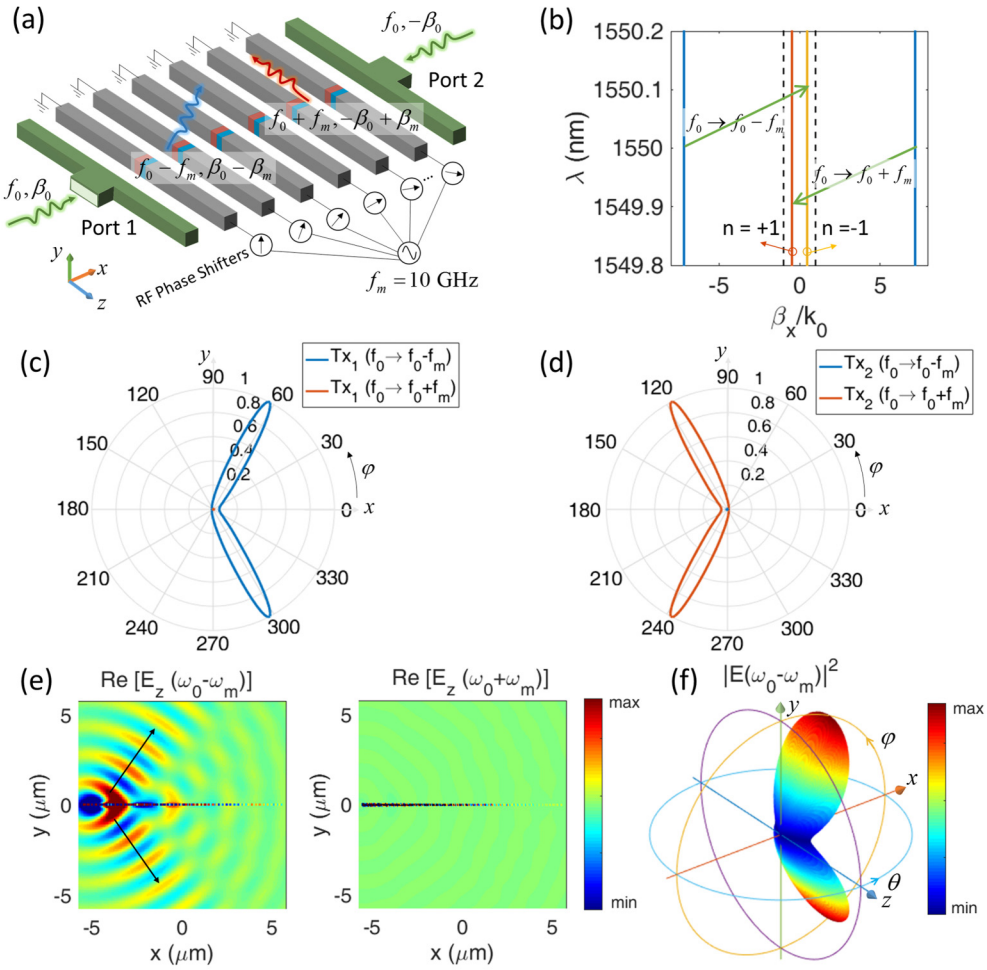

FIG. 6. (a) An array of plasmonic nanodipoles with spatiotemporal modulation, coupling injected guided modes into radiative leaky modes through space-time modal transitions. (b) The dispersion diagram of spatiotemporally modulated nanoantenna array and allowed space-time modal transitions for radiation of forward and backward propagating guided modes. (c) and (d) demonstrate the radiations patterns for first-order up- and down-modulated frequency harmonics corresponding to injection of backward guided mode from port 1 (forward propagating) and port 2 (backward propagating), respectively. (e) depicts the distributions of electric field corresponding to first-order up- and down-modulated frequency harmonics when the guided mode is injected from port 1. (f) three-dimensional radiation pattern of first-order down-modulated frequency harmonic for injection of a forward propagating guided mode.

of the dispersion diagram of Fig. 6(b). The input wave goes through space-time modal conversion as it propagates along the array in the $+x$ direction. It should be noted that the modal conversion to a specific space-time harmonic is not complete due to dissipation loss and intermodulation conversions. However, the long length chosen for the nanoantenna array ensures that all the modes are either radiated to the free space or decayed along the nanoantenna array before reaching the terminations. As such, the only contribution to the free-space radiation comes from the leaky modes. According to the Floquet theorem, the frequencies of the first-order allowed modes for conversion are $(f_0 - f_m, \beta_0 - \beta_m)$ and $(f_0 + f_m, \beta_0 + \beta_m)$. The first mode is accessible through branch $(n = -1)$ which lies within the leaky region while the second mode is accessible in the guided region. The space-time transition to the leaky mode is depicted in Fig. 6(b) by the arrow pointing toward up-right. As a result of this modal conversion, a bidirectional radiation of down-modulated frequency $(f_0 - f_m)$ is achieved in the H plane through uplink Tx_1 as shown in Fig. 6(c) while the contribution of up-modulated frequency harmonic to free-space radiation is negligibly small since it is a guided mode. The radiation angle can be theoretically obtained as [89]:

$$\phi_{t1} = \cos^{-1}\left(\frac{c(\beta_0 - \beta_m)}{\omega_0 - \omega_m}\right), \tag{17}$$

predicting $\phi_{t1} \approx \pm 62.13^\circ$ which is in excellent agreement with the radiation pattern shown in Fig. 6(c).

The input backward guided mode into port 2 with the same temporal frequency can be defined as $(f_0, -\beta_0)$ which lies on the right-hand side of the dispersion diagram. In this case, the first-order allowed modal transitions are $(f_0 - f_m, -\beta_0 - \beta_m)$ and $(f_0 + f_m, -\beta_0 + \beta_m)$ among which only the second mode is accessible within the leaky region. This transition is depicted by the arrow pointing toward down-left in the dispersion diagram of Fig. 6(b). As a result of this transition, a radiation of up-modulated frequency harmonic is achieved through uplink Tx_2 as shown in Fig. 6(d) toward the following

angle:

$$\phi_{t2} = \cos^{-1}\left(\frac{c(-\beta_0 + \beta_m)}{\omega_0 + \omega_m}\right), \tag{18}$$

which is calculated as $\phi_{t2} \approx \pm 117.87^\circ$ consistent with the bidirectional radiation pattern in Fig. 6(d).

The near-field distributions of the electric field corresponding to the first-order up- and down-modulated frequency harmonics are shown in Fig. 6(e) for the case of guided mode excitation from port 1. As can be seen, the down-modulated frequency harmonic shows a bidirectional radiation into free space while the up-modulated frequency harmonic is decayed along the array. The three-dimensional radiation pattern of the down-modulated frequency harmonic is also shown in Fig. 6(f) which demonstrates a directive pattern in the H plane, whereas in the E plane, the radiation pattern is roughly a dumbbell shape similar to a single dipole antenna.

The above analysis indicates the isolation of frequency between transmitted waves from port 1 and port 2 (uplinks) which is a result of nonreciprocal nature and directionality of the antenna. It should be noted that in principle, the nonreciprocity and asymmetry in the dispersion diagram of spatiotemporally modulated antenna can also largely break the symmetry between ϕ_{t1} and ϕ_{t2}, however, due to the fact that accessible modulation frequencies of electro-optical materials are very small compared to the excitation frequency in the NIR regime ($\omega_m \ll \omega_0$), the introduced asymmetry in the dispersion diagram is negligibly small and $\phi_1 \approx 180^\circ - \phi_2$.

Next, we investigate the Rx operation mode of the antenna. To this end, we illuminate the array with plane waves of different incident angles and measure the received powers at port 1 and port 2 as shown in Fig. 7(a). We consider the temporal frequency of incoming light as $f_0 - f_m$ which is the transmitting frequency of the antenna when it is fed from port 1. For a free-space mode with spatial frequency of β_x located in the radiation region, two photonic transitions are allowed into $(f_0 - 2f_m, \beta_x - \beta_m)$ and $(f_0, \beta_x + \beta_m)$. The first transition allows for efficient coupling to the backward propagating backward guided mode ($\beta_{x0} > 0$) on branch ($n = 0$), when the antenna is incident by the following angle:

$$\phi_{r1} = \cos^{-1}\left(-\frac{c\left(-\beta_0 + \beta_m - 2\omega_m \frac{d\beta_x}{d\omega}\right)}{\omega_0 - \omega_m}\right), \tag{19}$$

which is depicted in the dispersion diagram of Fig. 7(b) by the arrow pointing toward up-right. The second transition allows for efficient coupling to forward propagating backward guided mode ($\beta_{x0} < 0$) on branch ($n = 0$), when the antenna is incident by the following angle:

$$\phi_{r2} = \cos^{-1}\left(-\frac{c(\beta_0 - \beta_m)}{\omega_0 - \omega_m}\right), \tag{20}$$

which is shown in the dispersion diagram of Fig. 7(b) by the arrow pointing toward down-left. As such, the power is received through downlink Rx_1 with a frequency of $f_0 - 2f_m$ at port 1 when illuminated at an angle of $\phi_{r1} \approx \pm 62.13^\circ$ while it is received through downlink Rx_2 with a frequency of f_0 at port 2 when illuminated at an angle of $\phi_{r2} \approx \pm 117.87^\circ$. The reception patterns of port 1 and port 2 corresponding to up- and down-modulated frequency harmonics are shown in Figs. 7(c) and 7(d), respectively, which show an excellent agreement with the theoretically predicted values for the reception angles. It can be noted that the reception patterns are almost symmetric. This is due to the fact that, in the account of small modulation frequency, $\frac{\omega_m}{\omega_0} \ll \frac{d\omega}{d\beta}$ and thus $\phi_{r1} \approx 180^\circ - \phi_{r2}$. The near-field distributions of the electric field corresponding to the up- and down-modulated frequency harmonics are also shown in Figs. 7(e) and 7(f) for incident angles of ϕ_{r1} and ϕ_{r2}, respectively, which clearly show the reception of down- and up-modulated frequency harmonics at port 1 and port 2 through coupling to backward and forward propagating guided modes.

Comparing the transmission and reception performance of the array antenna in Figs. 6 and 7 clearly illustrates frequency isolation between transmission and reception modes (uplinks and downlinks) which rejects the interference of transmitted and received signals at each port of the antenna. Port 1 transmits and receives through down-conversion of frequency while port 2 up-converts the frequency of transmitted and received waves. It should be mentioned that, in addition to the isolation of Tx and Rx modes in the temporal domain, the spatiotemporal modulation can isolate the two modes in the spatial domain as well meaning that in principle the transmission and reception angles can be drastically different ($\phi_{t1} \neq \phi_{r1}$). However, due to the fact that in the NIR regime, the accessible modulation frequencies of electro-optical materials are very small compared to the optical frequency, $\frac{\omega_m}{\omega_0} \ll \frac{d\omega}{d\beta}$ and thus $\phi_{t1} \approx \phi_{r1}$. The spatial asymmetry between transmission and reception is the key to developing power isolators. In such applications, larger modulation frequencies can be obtained using optical modulation of carrier concentration in electro-optical materials [92] instead of electrical biasing. However, the focus of this paper has been on developing transceiver antennas requiring isolation of reception and transmission patterns in the temporal domain which can be accomplished using small modulation frequencies. In fact, the spatial symmetry of transmission and reception modes enables isolation of the transmitted and received signals propagating along the same direction at the same frequency through up- and down-conversion of frequency which is desirable in a full-duplex communication scheme [Fig. 1(c)]. In such a scenario, a three-port waveguide can be employed as a power divider/combiner as schematically shown in Fig. 8 which allows routing the input and output signals at different ports while the individual array antenna is serving the role of a full transceiver and rejects the interference between the signals.

C. Beam-scanning and antenna characteristics

In the following, we comprehensively study the characteristics of spatiotemporally modulated array antenna namely scanning angle, directivity, half-power beamwidth, radiation efficiency, and gain in terms of wavelength and spatial modulation frequency. It should be noted that the length of the leaky wave antennas chosen here (11 μm) is sufficiently long such that all the power is either radiated into free space or decayed along the array. As such, all the antenna characteristics are determined directly by the modal properties and wavelength.

In the account of electrical tunability of nanoantennas, both temporal (f_m) and spatial (β_m) modulation frequencies

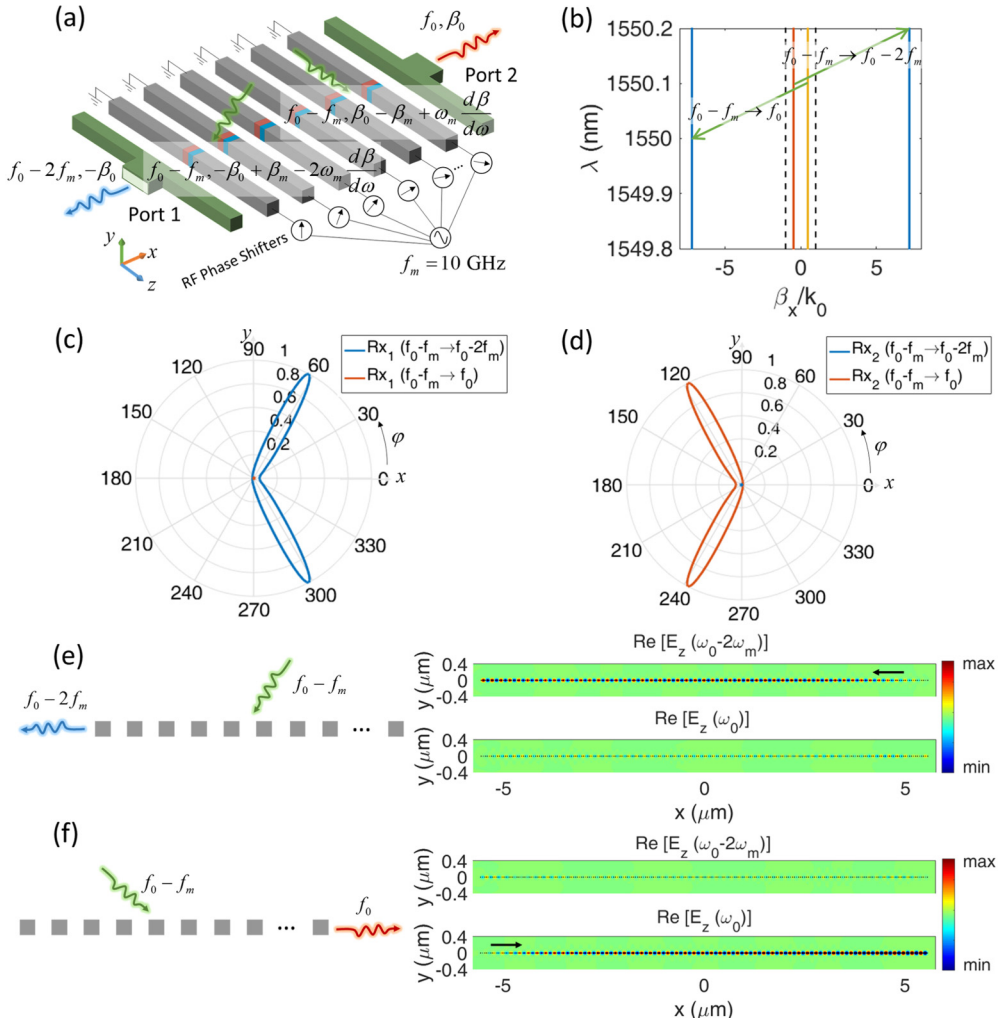

FIG. 7. (a) Spatiotemporally modulated nanoantenna array coupling incoming radiation into guided modes through space-time modal transitions. (b) Dispersion diagram of spatiotemporally modulated nanoantenna array and allowed space-time transitions for receiving the incoming radiation at port 1 (through backward propagating backward guided mode) and port 2 (through forward propagating backward guided mode). (c) and (d) demonstrate the reception patterns of the first-order up- and down-modulated harmonics at port 1 and port 2. (e) and (f) depict the distributions of electric field when the oblique incidence is coupled to backward and forward propagating backward guided modes of first-order frequency harmonics, respectively.

can be adjusted electrically to tune the transmission/reception frequency or scan the beam in real time. According to equations (17)–(20), the transmission and reception angles can be controlled through spatial modulation frequency (β_m) which is applied by the phase shifters in the RF biasing network. Figure 9(a) shows the beam-scanning functionality of array antenna in transmission of down-modulated frequency harmonics by changing β_m, when it is fed at port 1 (Tx_1 operation mode). All the radiation patterns are normalized with respect to peak gain to clearly demonstrate the scanning angles. An angle of view of 180° can be achieved in the beam scanning from backward endfire ($\phi = 180°$) to forward endfire ($\phi = 0°$).

The bandwidth of the transverse guided mode supported by the dense array of nanoantennas is enough to cover the entire C band. As such, the antenna can be used at different frequencies allowing to multiplex different communication channels into a single platform via dense wavelength division in order to increase the communication link capacity. The variation of beaming angle corresponding to the Tx_1 operation mode is shown in Fig. 9(b) as a function of wavelength and spatial modulation frequency. The dispersion of transverse backward guided mode yields $\frac{d\omega}{d\beta_x} < 0$ which leads to increment in the spatial frequency of guided mode β_0 by increasing the wavelength (decreasing the frequency). As such, the radiation angle in upper (lower) half space turns counterclockwise (clockwise) toward backward endfire by increasing the wavelength consistent with predicted values by equation (17) while the antenna preserves its functionality.

The directivity of radiation pattern corresponding to the Tx_1 operation mode is calculated using [1]:

$$D_t = \frac{2\pi |E_{\max}|^2}{\int_0^{2\pi} |E(\phi)|^2 d\phi}, \tag{21}$$

and the result is presented in Fig. 9(c) as a function of wavelength and spatial modulation frequency wherein the contours denote the corresponding beaming angles. It can be observed

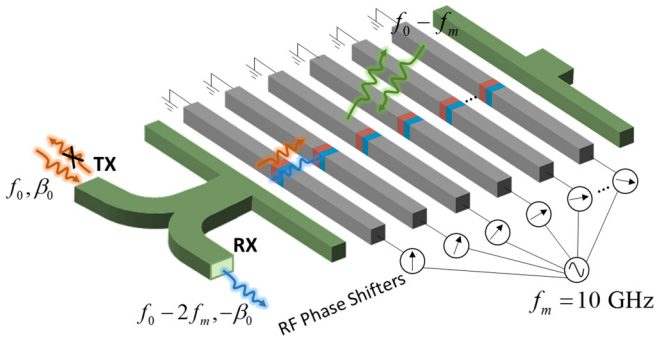

FIG. 8. A spatiotemporally modulated array antenna routing the transmitted and received signals propagating along the same direction at different paths through a three-port waveguide while rejecting the interference between this signals, thus, operating as a full transceiver.

that the variations of directivity are correlated with the beaming angle such that the maximal directivity corresponds to broadside angles ($\phi_{t1} = \pm 90^\circ$) while the directivity decreases as the beam approaches endfire direction ($\phi_{t1} = 0^\circ,\ 180^\circ$). Moreover, increasing the wavelength results into decrement of the directivity due to the increase in the imaginary part of guided mode's spatial frequency (attenuation constant).

The half-power beamwidth ($\Delta\phi_{3dB}$) of the radiation pattern is also obtained in terms of wavelength and spatial modulation frequency which is depicted in Fig. 9(d).

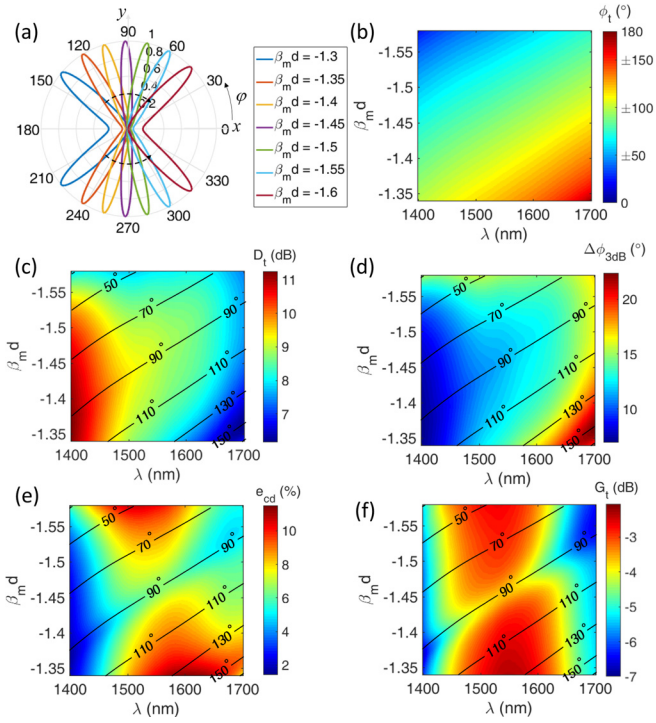

FIG. 9. (a) Electrical beam-scanning functionality of the array antenna in Tx_1 operation mode by adjusting the modulation phase delay. (b)–(f) demonstrate the beaming angle, directivity, half-power beamwidth, radiation efficiency, and gain of the array antenna as functions of wavelength and spatial modulation frequency in Tx_1 operation mode, respectively. The contours denote the beam angle.

The narrowest beamwidth corresponds to broadside and the width of the beam becomes wider as it approaches endfire which is consistent with the radiation patterns shown in Fig. 9(a).

The radiation efficiency of the antenna with respect to the input power depends on the feeding approach. Since the only contribution to the free-space radiation comes from modal transition of the guided mode; direct injection of the guided mode through a waveguide port leads to higher efficiency compared to the excitation with an external dipolar emitter. Here, we define the radiation efficiency (e_{cd}) with respect to the power accepted by the antenna at the input location, irrespective of the feeding approach. Figure 9(e) demonstrates the radiation power efficiency of the down-modulated frequency harmonic with respect to the received power at port 1 as a function of wavelength and spatial modulation frequency. As expected, the maximum radiation efficiency is obtained around the operating wavelength of $\lambda = 1.55\ \mu$m which corresponds to the resonant wavelength of nanoantennas. Moreover, the radiation efficiency increases as the beam approaches endfire while it exhibits a minimum at broadside. It should be mentioned that despite the enhancement of radiation efficiency around the resonance, the efficiency is still limited to less than 12% in the account of ohmic losses introduced by ITO and silver as well as imperfect modal transition to higher order frequency harmonics. It is noteworthy that the modal transition efficiency can be increased through decrement of modulation depth and increasing the interaction length which also results in larger dissipation loss [24]. As such, there is a tradeoff between the dissipation loss and modal conversion efficiency.

Finally, the antenna gain corresponding to the transmission in Tx_1 mode is obtained by multiplication of radiation efficiency and directivity ($G_t = e_{cd} D_t$) and the result is shown in Fig. 9(f) as a function of wavelength and spatial modulation frequency. As can be seen, a reasonably large gain is achieved over the entire C band around the resonant wavelength of nanoantennas. Similar results can be obtained for reception mode of the antenna which are not included for the sake of brevity.

IV. CONCLUSION

In summary, we have implemented time-modulated nanoantennas in the NIR frequency regime through integration of ITO into the gap of plasmonic nanodipoles and gate biasing with RF signals. We have also presented an extended DDA formulation to treat time-modulated systems with multiscale features in spatial and temporal domains based on a multifrequency approach and characterized electro-optical response of nanoantennas through linking of charge transport and electromagnetic models. The resonant characteristics of dipole nanoantennas lead to large confinement of electric field at the nanogap which enhances light-matter interactions with the ITO active region at nanoscale, yielding enhanced frequency conversion efficiencies. A spatiotemporally-modulated array antenna with leaky-wave architecture has been realized using an ensemble of separately biased nanoantennas with a progressive phase delay where the radiation is achieved via space-time

modal transitions of a guided mode. Nonreciprocal optical links have been established through up-conversion and down-conversion of the frequency which isolate the frequencies of transmitted and received signals at each port. The electrical beam-scanning functionality has been demonstrated and the dependence of the antenna characteristics to wavelength and modulation parameters has been studied comprehensively. This approach enables full-duplex communication through a shared transmission medium with an individual antenna at each communication node. Moreover, it allows for integration of multiplexing several wavelengths into a single transmission medium which can be exploited to increase the capacity of communication link.

ACKNOWLEDGMENT

This work is supported by the U.S. Air Force Office of Scientific Research (AFOSR), FA9550-14-1-0349 and FA9550-18-1-0354 in parts.

[1] C. A. Ballanis, *Antenna Theory Analysis and Design* (John Wiley and Son's Inc., New York, 1997).
[2] A. Alu and N. Engheta, Nat. Photon. **2**, 307 (2008).
[3] A. Alu and N. Engheta, Phys. Rev. Lett. **101**, 043901 (2008).
[4] P.-Y. Chen and A. Alù, Phys. Rev. B **82**, 235405 (2010).
[5] Y. Zhao, N. Engheta, and A. Alù, JOSA B **28**, 1266 (2011).
[6] A. Alù and N. Engheta, Phys. Rev. Lett. **104**, 213902 (2010).
[7] A. Ahmadi, S. Ghadarghadr, and H. Mosallaei, Opt. Express **18**, 123 (2010).
[8] T. Kosako, Y. Kadoya, and H. F. Hofmann, Nat. Photon. **4**, 312 (2010).
[9] X.-X. Liu and A. Alù, Phys. Rev. B **82**, 144305 (2010).
[10] C. A. Brackett, IEEE J. Sel. Areas Commun. **8**, 948 (1990).
[11] H. Toba, K. Oda, K. Nakanishi, N. Shibata, K. Nosu, N. Takato, and M. Fukuda, J. Lightwave Technol. **8**, 1396 (1990).
[12] M.-C. Tien, T. Mizumoto, P. Pintus, H. Kromer, and J. E. Bowers, Opt. Express **19**, 11740 (2011).
[13] Y. Hadad and B. Z. Steinberg, Opt. Express **21**, A77 (2013).
[14] Y. Hadad, A. R. Davoyan, N. Engheta, and B. Z. Steinberg, ACS Photonics **1**, 1068 (2014).
[15] S. Chen, F. Fan, X. Wang, P. Wu, H. Zhang, and S. Chang, Opt. Express **23**, 1015 (2015).
[16] D. L. Sounas and A. Alù, Nat. Photonics **11**, 774 (2017).
[17] M. Lawrence, D. R. Barton III, and J. A. Dionne, Nano Lett. **18**, 1104 (2018).
[18] D. R. Barton III, H. Alaeian, M. Lawrence, and J. Dionne, Phys. Rev. B **97**, 045432 (2018).
[19] C. Caloz, A. Alù, S. Tretyakov, D. Sounas, K. Achouri, and Z.-L. Deck-Léger, Phys. Rev. Appl. **10**, 047001 (2018).
[20] H. Lira, Z. Yu, S. Fan, and M. Lipson, Phys. Rev. Lett. **109**, 033901 (2012).
[21] D. L. Sounas, C. Caloz, and A. Alù, Nat. Commun. **4**, 2407 (2013).
[22] Y. Hadad, J. C. Soric, and A. Alu, Proc. Natl. Acad. Sci. **113**, 3471 (2016).
[23] S. Taravati and C. Caloz, IEEE Trans. Antennas Propag. **65**, 442 (2017).
[24] D. Correas-Serrano, J. Gomez-Diaz, D. Sounas, Y. Hadad, A. Alvarez-Melcon, and A. Alù, IEEE Antennas and Wireless Propagation Letters **15**, 1529 (2016).
[25] Y. Hadad, D. L. Sounas, and A. Alu, Phys. Rev. B **92**, 100304(R) (2015).
[26] A. Shaltout, A. Kildishev, and V. Shalaev, Opt. Mater. Express **5**, 2459 (2015).
[27] S. Taravati, B. A. Khan, S. Gupta, K. Achouri, and C. Caloz, IEEE Trans. Antennas Propag. **65**, 3589 (2017).
[28] Y. Shi, S. Han, and S. Fan, ACS Photonics **4**, 1639 (2017).
[29] M. M. Salary, S. Jafar-Zanjani, and H. Mosallaei, Phys. Rev. B **97**, 115421 (2018).
[30] M. M. Salary, S. Jafar-Zanjani, and H. Mosallaei, New J. Phys. **20**, 123023 (2018).
[31] S. Inampudi, M. M. Salary, S. Jafar-Zanjani, and H. Mosallaei, Opt. Mater. Express **9**, 162 (2019).
[32] M. G. Wood, S. Campione, S. Parameswaran, T. S. Luk, J. R. Wendt, D. K. Serkland, and G. A. Keeler, Optica **5**, 233 (2018).
[33] Y.-W. Huang, H. W. H. Lee, R. Sokhoyan, R. A. Pala, K. Thyagarajan, S. Han, D. P. Tsai, and H. A. Atwater, Nano Lett. **16**, 5319 (2016).
[34] J. Park, J.-H. Kang, S. J. Kim, X. Liu, and M. L. Brongersma, Nano Lett. **17**, 407 (2016).
[35] M. M. Salary and H. Mosallaei, Sci. Rep. **7**, 10055 (2017).
[36] S. J. Kim and M. L. Brongersma, Opt. Lett. **42**, 5 (2017).
[37] A. Forouzmand, M. M. Salary, S. Inampudi, and H. Mosallaei, Adv. Opt. Mater. **6**, 1701275 (2018).
[38] M. L. Brongersma, J. W. Hartman, and H. A. Atwater, Phys. Rev. B **62**, R16356(R) (2000).
[39] A. Alù and N. Engheta, Phys. Rev. B **74**, 205436 (2006).
[40] Y. Hadad and B. Z. Steinberg, Phys. Rev. Lett. **105**, 233904 (2010).
[41] A. B. Evlyukhin, C. Reinhardt, and B. N. Chichkov, Phys. Rev. B **84**, 235429 (2011).
[42] A. L. Fructos, S. Campione, F. Capolino, and F. Mesa, JOSA B **28**, 1446 (2011).
[43] A. B. Evlyukhin, C. Reinhardt, E. Evlyukhin, and B. N. Chichkov, JOSA B **30**, 2589 (2013).
[44] M. M. Salary, A. Forouzmand, and H. Mosallaei, ACS Photonics **4**, 63 (2016).
[45] Y. Mazor and B. Z. Steinberg, Phys. Rev. B **94**, 235114 (2016).
[46] X.-X. Liu, Y. Zhao, and A. Alù, IEEE Trans. Antennas Propag. **64**, 2301 (2016).
[47] P. C. Chaumet, A. Sentenac, and A. Rahmani, Phys. Rev. E **70**, 036606 (2004).
[48] F. M. Kahnert, J. Quant. Spectrosc. Radiat. Transfer **79**, 775 (2003).
[49] M. A. Yurkin and A. G. Hoekstra, J. Quant. Spectrosc. Radiat. Transfer **106**, 558 (2007).
[50] M. I. Mishchenko, V. P. Tishkovets, L. D. Travis, B. Cairns, J. M. Dlugach, L. Liu, V. K. Rosenbush, and N. N. Kiselev, J. Quant. Spectrosc. Radiat. Transfer **112**, 671 (2011).
[51] M. A. Yurkin and A. G. Hoekstra, J. Quant. Spectrosc. Radiat. Transfer **112**, 2234 (2011).

[52] E. M. Purcell and C. R. Pennypacker, Astrophys. J. **186**, 705 (1973).
[53] B. T. Draine and P. J. Flatau, JOSA A **11**, 1491 (1994).
[54] B. T. Draine and J. Goodman, Astrophys. J. **405**, 685 (1993).
[55] X.-B. Xu, Z. Yi, X.-B. Li, Y.-Y. Wang, X. Geng, J.-S. Luo, B.-C. Luo, Y.-G. Yi, and Y.-J. Tang, J. Phys. Chem. C **116**, 24046 (2012).
[56] See Supplemental Material at http://link.aps.org/supplemental/10.1103/PhysRevB.99.045416 for further details on derivation of DDA equations from VIE formulation of Maxwell's equations, validation of multifrequency DDA via full-wave FDTD simulations, model order reduction based on dynamic polarizability, and multifrequency dynamic polarizability of time-modulated nanoantennas.
[57] Y. Zhao, N. Engheta, and A. Alù, Metamaterials **5**, 90 (2011).
[58] B. Zhang, G. Xiao, J. Mao, and Y. Wang, IEEE Trans. Antennas Propag. **58**, 3576 (2010).
[59] L. Hu, L.-W. Li, and R. Mittra, IEEE Trans. Antennas Propag. **58**, 3086 (2010).
[60] A. Rashidi, H. Mosallaei, and R. Mittra, J. Appl. Phys. **109**, 123109 (2011).
[61] D. Ansari Oghol Beig and H. Mosallaei, Prog. Electromagn. Res. **43**, 211 (2012).
[62] S. A. Tretyakov, F. Mariotte, C. R. Simovski, T. G. Kharina, and J.-P. Heliot, IEEE Trans. Antennas Propag. **44**, 1006 (1996).
[63] R. Marqués, F. Mesa, J. Martel, and F. Medina, IEEE Trans. Antennas Propag. **51**, 2572 (2003).
[64] A. Ishimaru, S.-W. Lee, Y. Kuga, and V. Jandhyala, IEEE Trans. Antennas Propag. **51**, 2550 (2003).
[65] F. B. Arango and A. F. Koenderink, New J. Phys. **15**, 073023 (2013).
[66] Y. Shi, W. Shin, and S. Fan, Optica **3**, 1256 (2016).
[67] J. Goodman, B. T. Draine, and P. J. Flatau, Opt. Lett. **16**, 1198 (1991).
[68] D. Ansari-Oghol-Beig, M. Rostami, E. Chernobrovkina, S. K. Saikin, S. Valleau, H. Mosallaei, and A. Aspuru-Guzik, J. Appl. Phys. **114**, 164315 (2013).
[69] S. Campione and F. Capolino, Radio Sci. **47**, RS0N06 (2012).
[70] Y. P. Chen, E. Wei, W. C. Choy, L. Jiang, and W. C. Chew, Opt. Express **20**, 20210 (2012).
[71] J.-Y. Ou, E. Plum, J. Zhang, and N. I. Zheludev, Nat. Nanotechnol. **8**, 252 (2013).
[72] M. J. Dicken, K. Aydin, I. M. Pryce, L. A. Sweatlock, E. M. Boyd, S. Walavalkar, J. Ma, and H. A. Atwater, Opt. Express **17**, 18330 (2009).
[73] Y.-J. Lu, R. Sokhoyan, W.-H. Cheng, G. K. Shirmanesh, A. R. Davoyan, R. A. Pala, K. Thyagarajan, and H. A. Atwater, Nat. Commun. **8**, 1631 (2017).
[74] G. Kafaie Shirmanesh, R. Sokhoyan, R. A. Pala, and H. A. Atwater, Nano Lett. **18**, 2957 (2018).
[75] G. Chen, H. Chen, M. Haurylau, N. A. Nelson, D. H. Albonesi, P. M. Fauchet, and E. G. Friedman, Integration, the VLSI journal **40**, 434 (2007).
[76] S. Edalatpour, M. Čuma, T. Trueax, R. Backman, and M. Francoeur, Phys. Rev. E **91**, 063307 (2015).
[77] N. B. Piller, Opt. Lett. **22**, 1674 (1997).
[78] P. B. Johnson and R.-W. Christy, Phys. Rev. B **6**, 4370 (1972).
[79] F. Michelotti, L. Dominici, E. Descrovi, N. Danz, and F. Menchini, Opt. Lett. **34**, 839 (2009).
[80] F. Yi, E. Shim, A. Y. Zhu, H. Zhu, J. C. Reed, and E. Cubukcu, Appl. Phys. Lett. **102**, 221102 (2013).
[81] A. Klein, C. Körber, A. Wachau, F. Säuberlich, Y. Gassenbauer, S. P. Harvey, D. E. Proffit, and T. O. Mason, Materials **3**, 4892 (2010).
[82] S. A. Maier, P. G. Kik, and H. A. Atwater, Appl. Phys. Lett. **81**, 1714 (2002).
[83] L. Zhao, K. L. Kelly, and G. C. Schatz, J. Phys. Chem. B **107**, 7343 (2003).
[84] I. Romero, J. Aizpurua, G. W. Bryant, and F. J. G. De Abajo, Opt. Express **14**, 9988 (2006).
[85] W. Zhang, Q. Li, and M. Qiu, Opt. Express **21**, 172 (2013).
[86] Y. Ren, Q. Chen, H. Qi, L. Ruan, and J. Dai, Int. J. Heat Mass Transf. **127**, 244 (2018).
[87] S. A. Maier, M. L. Brongersma, P. G. Kik, S. Meltzer, A. A. Requicha, and H. A. Atwater, Adv. Mater. **13**, 1501 (2001).
[88] Q. Song, S. Campione, O. Boyraz, and F. Capolino, Opt. Express **19**, 8735 (2011).
[89] F. Monticone and A. Alu, Proc. IEEE **103**, 793 (2015).
[90] J. R. Zurita-Sánchez, P. Halevi, and J. C. Cervantes-Gonzalez, Phys. Rev. A **79**, 053821 (2009).
[91] D. K. Kalluri, *Electromagnetics of Time Varying Complex Media: Frequency and Polarization Transformer* (CRC Press, Boca Raton, 2016).
[92] M. Abb, P. Albella, J. Aizpurua, and O. L. Muskens, Nano Lett. **11**, 2457 (2011).